

than 10 in supernova remnant shocks, and $M_A > 20$ have been observed at Saturn's bow shock (3, 27). The present results indicate that, in such strong shock waves, the upstream (ion) kinetic energy can be converted to magnetic energy, which will be further dissipated efficiently via turbulent reconnection. The resulting reconnection jets and magnetic islands work as scattering bodies, akin to the role played by Alfvén waves in the cosmic-ray transport theory (28, 29).

REFERENCES AND NOTES

1. A. Bamba, R. Yamazaki, M. Ueno, K. Koyama, *Astrophys. J.* **589**, 827–837 (2003).
2. F. Acero et al., *Astron. Astrophys.* **516**, A62 (2010).
3. A. Masters et al., *Nat. Phys.* **9**, 164–167 (2013).
4. S. Masuda, T. Kosugi, H. Hara, S. Tsuneta, Y. Ogawara, *Nature* **371**, 495–497 (1994).
5. R. P. Lin et al., *Astrophys. J.* **595**, L69–L76 (2003).
6. M. Ølsgaard, R. P. Lin, T. D. Phan, D. E. Larson, S. D. Bale, *Phys. Rev. Lett.* **89**, 195001 (2002).
7. S. Imada et al., *J. Geophys. Res.* **112**, A03202 (2007).
8. K. G. McClements, M. E. Dieckmann, A. Ynnerman, S. C. Chapman, R. O. Dendy, *Phys. Rev. Lett.* **87**, 255002 (2001).
9. M. Hoshino, N. Shimada, *Astrophys. J.* **572**, 880–887 (2002).
10. J. F. Drake et al., *Science* **299**, 873–877 (2003).
11. J. Egedal, W. Daughton, A. Le, *Nat. Phys.* **8**, 321–324 (2012).
12. M. M. Leroy, *Phys. Fluids* **26**, 2742 (1983).
13. C. Wu et al., *Space Sci. Rev.* **37**, 63 (1984).
14. K. Papadopoulos, *Astrophys. Space Sci.* **144**, 535 (1988).
15. P. J. Cargill, K. Papadopoulos, *Astrophys. J.* **329**, L29 (1988).
16. T. Amano, M. Hoshino, *Astrophys. J.* **690**, 244–251 (2009).
17. M. A. Riquelme, A. Spitkovsky, *Astrophys. J.* **733**, 63 (2011).
18. Y. Matsumoto, T. Amano, M. Hoshino, *Astrophys. J.* **755**, 109 (2012).
19. B. D. Fried, *Phys. Fluids* **2**, 337 (1959).
20. J. T. Frederiksen, C. B. Heddal, T. Haugbølle, Å. Nordlund, *Astrophys. J.* **608**, L13–L16 (2004).
21. T. N. Kato, H. Takabe, *Astrophys. J.* **681**, L93–L96 (2008).
22. T. N. Kato, H. Takabe, *Astrophys. J.* **721**, 828–842 (2010).
23. Y. Matsumoto, T. Amano, M. Hoshino, *Phys. Rev. Lett.* **111**, 215003 (2013).
24. M. Hoshino, *Phys. Rev. Lett.* **108**, 135003 (2012).
25. J. F. Drake, M. Swisdak, H. Che, M. A. Shay, *Nature* **443**, 553–556 (2006).
26. G. Kowal, E. M. de Gouveia Dal Pino, A. Lazarian, *Astrophys. J.* **735**, 102 (2011).
27. A. Masters et al., *J. Geophys. Res.* **116**, A10107 (2011).
28. E. Fermi, *Phys. Rev.* **75**, 1169–1174 (1949).
29. J. Skilling, *Mon. Not. R. Astron. Soc.* **172**, 557–566 (1975).

ACKNOWLEDGMENTS

This research used the computational resources of the K computer provided by the RIKEN Advanced Institute for Computational Science through the High Performance Computing Infrastructure System Research project (project identification nos. hp120222 and hp120287) and was supported in part by a Japan Society for the Promotion of Science KAKENHI Grant-in-Aid for Scientific Research (C) 26400266, Ministry of Education, Culture, Sports, Science and Technology Strategic Programs for Innovative Research and the Joint Institute for Computational Fundamental Science.

SUPPLEMENTARY MATERIALS

www.sciencemag.org/content/347/6225/974/suppl/DC1
Movie S1

19 August 2014; accepted 3 February 2015
10.1126/science.1260168

SURFACE CHEMISTRY

Probing the transition state region in catalytic CO oxidation on Ru

H. Öström,¹ H. Öberg,¹ H. Xin,² J. LaRue,^{2,3} M. Beye,^{2,4} M. Dell'Angela,⁵ J. Gladh,¹ M. L. Ng,² J. A. Sellberg,^{1,2} S. Kaya,² G. Mercurio,⁵ D. Nordlund,⁶ M. Hantschmann,⁴ F. Hieke,⁵ D. Kühn,⁴ W. F. Schlottter,⁷ G. L. Dakovski,⁷ J. J. Turner,⁷ M. P. Minitti,⁷ A. Mitra,⁷ S. P. Moeller,⁷ A. Föhlisch,^{4,8} M. Wolf,⁹ W. Wurth,^{5,10} M. Persson,¹¹ J. K. Nørskov,^{2,3} F. Abild-Pedersen,² H. Ogasawara,⁶ L. G. M. Pettersson,¹ A. Nilsson^{1,2,6*}

Femtosecond x-ray laser pulses are used to probe the carbon monoxide (CO) oxidation reaction on ruthenium (Ru) initiated by an optical laser pulse. On a time scale of a few hundred femtoseconds, the optical laser pulse excites motions of CO and oxygen (O) on the surface, allowing the reactants to collide, and, with a transient close to a picosecond (ps), new electronic states appear in the O K-edge x-ray absorption spectrum. Density functional theory calculations indicate that these result from changes in the adsorption site and bond formation between CO and O with a distribution of OC–O bond lengths close to the transition state (TS). After 1 ps, 10% of the CO populate the TS region, which is consistent with predictions based on a quantum oscillator model.

The transition state (TS) is the key to understanding chemical reactivity (1). It separates reactants from products, and the free energy required to reach it determines the kinetics of an elementary chemical reaction. Molecules in the TS are hard to capture or observe because the short lifetime leads to a near-zero TS population at steady-state conditions. Ultrafast pump-probe techniques have, however, opened up opportunities for probing molecular structures near the TS region by promoting a sufficient population of molecules to allow detection on short time scales (1, 2). In particular, a number of dissociation and isomerization processes of single molecular units have been probed with visible and infrared laser pulses (1). Much of chemistry, however, involves bimolecular reactions where new chemical bonds are formed. Previous pump-probe experiments have been performed in cases where reactants in the gas phase are brought together as a van der Waals complex or in liquid phase reactions between

solute and solvent. These experiments could follow the bimolecular reaction dynamics and detect intermediates, but a direct spectroscopic probing of the TS region has proved a challenge (3–5). We take the next step and probe the TS region through time-resolved snapshots of the valence electronic structure in a surface-catalyzed bimolecular reaction.

A catalyst modifies the TS substantially, opening new reaction pathways that can lead to higher reactivity and selectivity (6, 7). Furthermore, the surface in heterogeneous catalysis and the metal center in homogeneous catalysis both facilitate the reaction by bonding the reacting molecular fragments in close proximity. This opens up the prospect of probing bimolecular reactions on ultrafast time scales where the reacting adsorbed species are present at neighboring sites and are brought to collide rapidly by optical excitation. Optical lasers can drive surface reactions on ultrafast time scales (8–14) and, in particular, the reaction between adsorbed CO and O to form CO₂ on metal surfaces, which occurs within a few picoseconds (ps) (11, 12, 14). The ability to probe species on surfaces on ultrafast time scales has recently taken a major leap forward with the development of free-electron x-ray lasers delivering ultrashort pulses combined with atom-specific spectroscopic tools to monitor the electronic structure (15–17). In a first exploitation of this technique, a short-lived intermediate precursor state was detected in CO desorption from Ru using x-ray emission spectroscopy (XES) and x-ray absorption spectroscopy (XAS) (16).

We demonstrate that ultrafast pump-probe x-ray spectroscopy based on the Linac Coherent Light Source (LCLS) x-ray free-electron laser (18) can be used to probe the electronic structure of molecular species in the TS region during CO oxidation on a Ru surface. With an optical laser pump pulse, we excited the electrons in the substrate. Subsequent energy transfer to the adsorbate

¹Department of Physics, AlbaNova University Center, Stockholm University, SE-10691, Sweden. ²SUNCAT Center for Interface Science and Catalysis, SLAC National Accelerator Laboratory, 2575 Sand Hill Road, Menlo Park, CA 94025, USA. ³SUNCAT Center for Interface Science and Catalysis, Department of Chemical Engineering, Stanford University, Stanford, CA 95305, USA. ⁴Helmholtz Zentrum Berlin für Materialien und Energie GmbH, Albert-Einstein-Strasse 15, D-12489 Berlin, Germany. ⁵Physics Department and Center for Free Electron Laser Science, University of Hamburg, Luruper Chaussee 149, D-22761 Hamburg, Germany. ⁶Stanford Synchrotron Radiation Lightsource, SLAC National Accelerator Laboratory, 2575 Sand Hill Road, Menlo Park, CA 94025, USA. ⁷Linac Coherent Light Source, SLAC National Accelerator Laboratory, 2575 Sand Hill Road, Menlo Park, CA 94025, USA. ⁸Fakultät für Physik und Astronomie, Universität Potsdam, Karl-Liebknecht-Strasse 24-25, 14476 Potsdam, Germany. ⁹Fritz-Haber Institute of the Max-Planck-Society, Faradayweg 4-6, D-14195 Berlin, Germany. ¹⁰Deutsches Elektronen-Synchrotron, Photon Science, Notkestrasse 85, D-22607 Hamburg, Germany. ¹¹Surface Science Research Centre and Department of Chemistry, The University of Liverpool, Liverpool, L69 3BX, UK.

*Corresponding author. E-mail: nilsson@slac.stanford.edu

system led to a rapid increase in adsorbate-substrate vibrational excitations, which then drove the CO oxidation reaction on ultrafast time scales. Using O K-edge XAS, we followed the time evolution of the unoccupied valence electronic structure around the adsorbed O and CO in an element-specific way during the oxidation process. Both the O and CO adsorbed species were activated within a few hundred femtoseconds upon laser excitation. This result suggests an ultrafast energy transfer to the adsorbed species from surface electrons excited by the laser pulse. After a delay on the order of 800 fs, new electronic states appeared, indicating the existence of new adsorbed species that do not resemble the separate systems in terms of CO molecules or O atoms adsorbed on the Ru surface. By comparing the experimental data to calculations of XAS spectra, these new resonances are identified as due to CO shifted from on-top toward hollow sites, O from hollow sites toward bridge sites, and the formation of a bond between CO and O that is substantially elongated in comparison to the CO₂ final product. From the computed potential energy surface for the reaction, these fragments can be identified as molecular species being in the TS region while attempting to form CO₂. Based on a simple quantum mechanical

picture, we provide a probability analysis that rationalizes the ~10% population of species in the TS region during the first few ps as indicated by the experiment.

The black curve in Fig. 1A shows the initial ($t < 0$ ps) unpumped XAS O K-edge spectrum of atomic O and CO coadsorbed on Ru(0001) (17, 19). The resonance at 530.8 eV is the signature of the adsorbed O atom as an O $2p$ -Ru $4d$ antibonding state, here denoted O $2p^*$, that resides just above the Fermi level (20). The spectral feature at 533.8 eV is the $2\pi^*$ resonance of adsorbed CO (16, 21), and the broad structure at 542 eV is related to adsorbed O as an O $2p$ -Ru $5sp$ shape resonance (22).

With a delay of ~1 ps after excitation by a 400-nm laser pulse, the XAS spectrum changed dramatically, as shown in red in Fig. 1A. We observed four distinct major spectral changes with respect to the unpumped spectrum. These changes were visualized in more detail after curve-fitting the pumped spectrum with four new spectral components, together with 90% of the unpumped spectrum; to account for the increased translational, nonreactive motion, the position of the CO $2\pi^*$ level was let free and shifted to lower energy, similar to the case of pure CO on Ru(0001) after 400-nm laser excitation (15). We observed a low-energy component at 529.8 eV in the

O-related O $2p^*$ feature, indicating activation of the O atoms. Additional intensity appeared between the O $2p^*$ and CO $2\pi^*$ resonances at 532 eV that was neither present upon laser excitation of CO adsorbed separately on Ru(0001) (15) nor seen in spectrum calculations of O displacement toward lower coordination in the coadsorbate system. We saw a shoulder on the high-energy side of the $2\pi^*$ resonance distinguished more clearly in the curve fitting as a broad resonance at 535.6 eV, and there was additional intensity appearing at higher energies that could be approximated as a broad feature centered at 539 eV. The intensity in this region was fitted with two separate Gaussians in order to incorporate the features predicted from our spectrum calculations.

Figure 1B shows the transient changes of these spectral features in terms of delay from the laser pump (19). Despite the shot-by-shot statistical uncertainties in the x-ray spectra with spurious effects already before the optical pulse, significant and systematic changes are evident in Fig. 1B. The O $2p^*$ intensity shows a rapid increase on a 280 ± 100 fs time scale (19), which can be regarded as almost instantaneous within our time resolution. This time scale is similar to the thermalization time of femtosecond laser-excited electrons in Ru (23), such that both thermalized and nonthermalized electrons may contribute (8, 17). The shift in the CO $2\pi^*$ occurs on a time scale of 550 ± 120 fs, and the new state between the O $2p^*$ and CO $2\pi^*$ appears on the same 800 ± 250 fs time scale as the additional intensity in the region 536 to 539 eV (19).

To shed more light on the molecular species that give rise to these additional spectral features, we turn to density functional theory calculations of XAS spectra (19, 24) based on structures found along the minimum energy reaction path. Figure 2A shows the calculated pathway from the initial state (IS), where the CO is adsorbed at an on-top site and O in a hollow site, to the highest TS (TS1), where O and CO have come into chemical contact with the O atom in the bridge site and CO in a near-hollow site with a small 16° tilt from the surface normal. Beyond TS1, we find a rather flat descending region that ends with an abrupt change in energy, giving a small barrier (TS2), which corresponds to a bent, weakly chemisorbed CO₂ species that has a 34° tilt and where, along the CO-O reaction coordinate, there is still a bond elongation in comparison to the expected final state (FS), with CO₂ released into gas phase with substantial kinetic energy (25). To analyze the reaction further, we compute the potential of mean force (16), including contributions from entropy, as a function of the reaction coordinate. Figure 2A shows that TS1 and TS2 become stabilized relative to the IS at higher temperatures, but otherwise there are no dramatic changes.

Figure 2, B and C, show the calculated O K-edge spectra of O and CO along the reaction path. In Fig. 2C, we observe a red-shifted O $2p^*$ peak for O in a near-bridge position, which we relate to the intensity at 529.8 eV in the experiment. Focusing

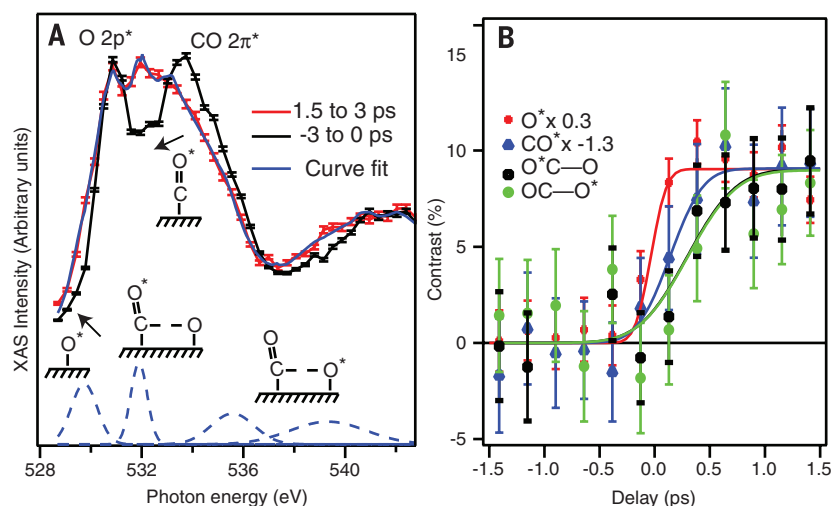


Fig. 1. Measured x-ray absorption spectra with time-dependent changes. (A) Pump-probe O K-edge XAS spectrum of CO/O/Ru(0001). The black line and markers show as reference the spectrum averaged over the 3 ps right before the arrival of the pump pulse, and the red line and markers show the spectrum averaged over the interval between 1.5 and 3 ps after the arrival of the laser pump. Averaging is performed to reduce noise. The solid blue line shows a curve fit obtained from a weighted sum of the unpumped XAS spectrum and the four Gaussians plotted with dashed blue lines in the bottom of the figure, with a red shift of the CO $2\pi^*$ due to external vibrational motion taken into account. The insets schematically depict the microscopic interpretation of the laser-induced spectral changes, and the arrows indicate the direction of spectral shifts as the O and CO species move out from their equilibrium sites. (B) Time development of the spectral intensities in four different spectral regions plotted as the contrast [difference between the pumped and unpumped experimental data normalized to the sum of the intensities and scaled to have the same asymptotes (19)]. The red dots (O*) show the contrast on the low-energy side of the O $2p^*$ that corresponds to activation of adsorbed O. Note the very fast (280 fs) change in contrast following the pump laser. The blue triangles (CO*) show the contrast on the CO $2\pi^*$ resonance, where a negative contrast appears on a 550-fs time scale [reversed in the figure for easy comparison of slopes (19)], corresponding to a loss of intensity after laser irradiation due to activation of external vibrations in the adsorbed CO. The black squares (O*-C-O*) and green circles (OC-O*) show the contrast around the O-CO π^* and O-CO σ^* , respectively. Both show a transient increase in the contrast on a time scale of 800 fs. The Poisson error bars are shown.

on the changes between IS and TS1, Fig. 2B shows a shift of 1 eV in the CO $2\pi^*$ position toward lower energy, into the region between the O and CO

resonances, where we observed an increase in intensity in the experimental data. Such a shift has been established previously for CO on Ni(100),

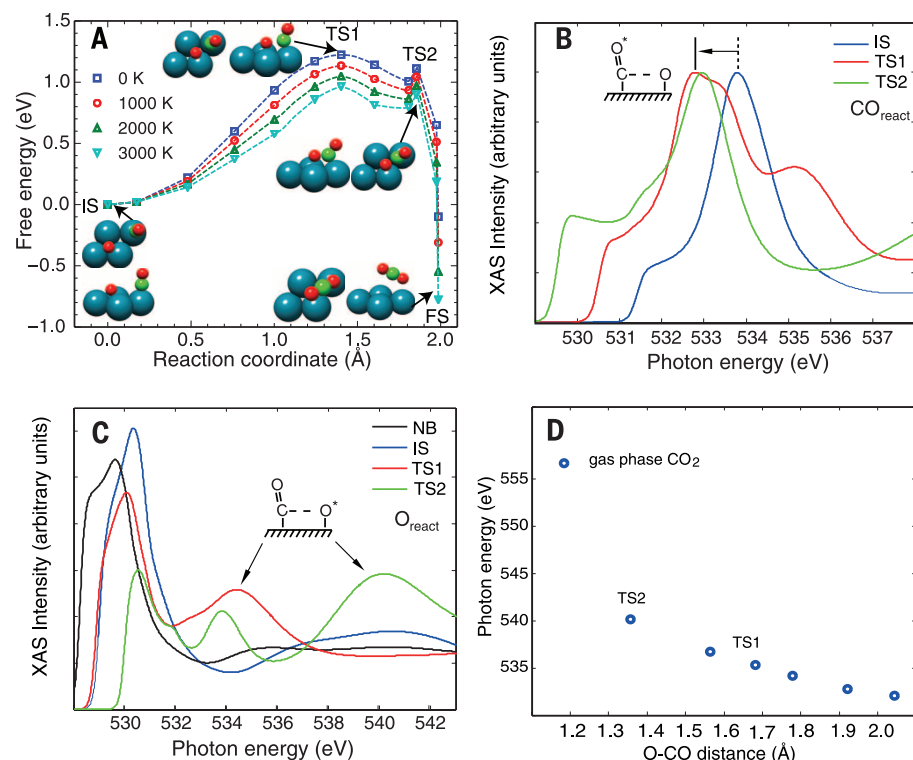


Fig. 2. Computed reaction path and x-ray spectra. (A) The free energy for CO oxidation on Ru(0001) at 0 K (minimum energy path), 1000 K, 2000 K, and 3000 K. To put the initial state (IS) structure at the origin, the reaction coordinate is defined as $d_{\text{O-CO}}(\text{IS}) - d_{\text{O-CO}}(X)$, where $d_{\text{O-CO}}$ is the distance between the reacting O atom and the C atom in the adsorbed CO molecule, and X is the position along the reaction path, from the IS to the final state (FS). The surface structures (top and side view) of the IS, TS1, TS2, and FS are shown. (B and C) Computed XAS O K-edge spectra of selected geometries projected on the reacting CO (B) or O (C). In (C), the XAS spectrum for a separate configuration denoted NB (near-bridge) in which atomic O is situated close to a bridge site in the coadsorbate system is also shown. (D) The computed energy of the shape resonance (see Fig. 2C, where it is mainly located on the O atom at ~540 eV in TS2) arising from OC-O bond formation is plotted against the OC-O bond length for a number of different geometries along the reaction path. The linear trend is broken as the resonance position of gas phase CO₂ is included at ~557 eV.

where coadsorbed hydrogen generates a mixed on-top and hollow phase where the experimental XAS spectrum shows a shift of 2 eV between the two adsorption sites (26). This result is similar to the O 1s binding energy shift observed with x-ray photoelectron spectroscopy (27). The computed shift is consistent with the present experimental data but seems to be underestimated. The CO $2\pi^*$ shift is similar for TS2. We denote this spectral component O^{*}C-O, because it is the O atom in the CO molecule that mostly contributes the spectral intensity.

In TS1, a weak OC-O bond is formed with an elongated bond distance of 1.7 Å, compared with 1.2 Å in the CO₂ molecule. The sigma bond within a molecule gives rise to an antibonding shape resonance whose energy position is sensitive to the bond length (28). In Fig. 2C, we note that the computed OC-O^{*} shape resonance, mostly located on the O atom, is at 535.5 eV, which nicely corresponds to the intensity appearing on the high-energy side of the CO $2\pi^*$ resonance after the laser pump. Figure 2C shows that this resonance shifts to higher energy at 540 eV in the TS2 state because of a shorter OC-O bond length. There is not much contribution in the pumped experimental data at 540 eV indicating less population of TS2, but, as discussed above, there is substantial intensity around 538 to 539 eV indicating species with bond lengths between TS1 and TS2. Figure 2D shows a nearly linear dependence between bond length and resonance position in the computed OC-O shape resonance energy position until the bond length becomes similar to the other internal C-O bond and the two resonances delocalize (28), as seen in CO₂. Because the pumped spectra from Fig. 1 can be fit with two broad OC-O resonances, there are species of various bond lengths contributing to the experimental data. This corresponds to the population of several points around TS1 and on the path toward TS2 as the activated species undergo several attempts to react, where the majority does not pass over the barrier, however, but dissociate back to O and CO.

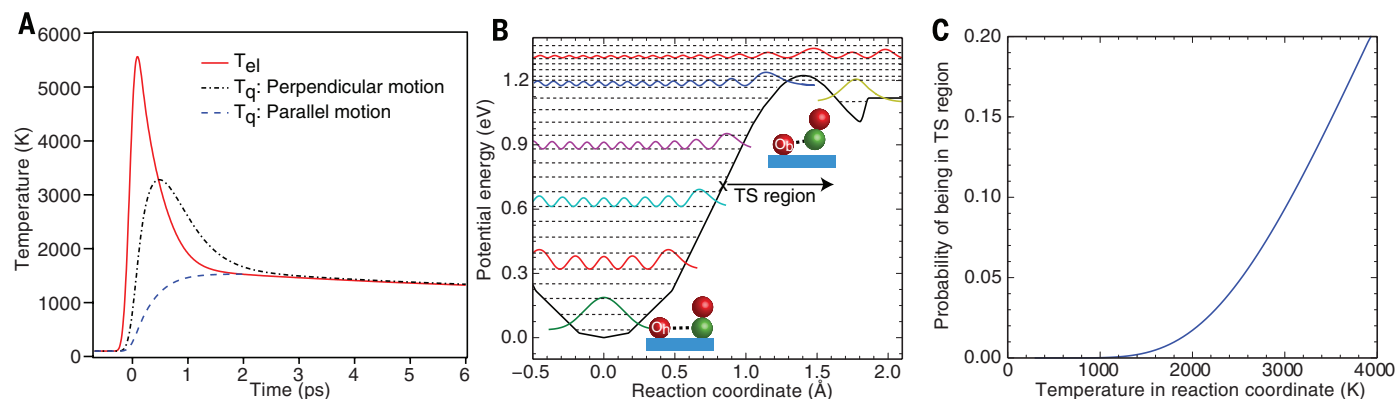
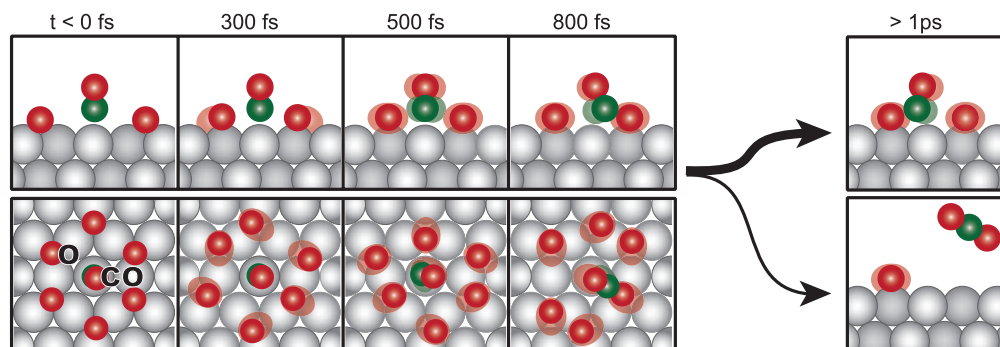


Fig. 3. Time evolution of the temperature and probability analysis for forming O-CO near-TS complexes on Ru(0001). (A) Based on the two-temperature model and ab initio electronic friction of O atoms on Ru(0001) (19), the peak values of the adsorbate temperature in the relevant O-Ru vibrational modes perpendicular and parallel to the surface are estimated to be 1500 to 3300 K in the time range between 0.5 and 3 ps after the laser excitation. (B) Minimum energy path for CO oxidation where the left side,

approaching a different O atom, is not shown for simplicity (19). Dashed lines are energy eigenvalues, and solid lines represent the corresponding probability density distribution at selected energy levels. The TS region is defined by the inflection point (arrow) of the minimum energy path out to 2 Å. (C) Probability of finding O-CO complexes within the TS region as a function of the adsorbate temperature in the reaction coordinate. The peak values of the adsorbate temperature lead to a potential population of the TS region of up to ~10%.

Fig. 4. Pictorial side and top views of the reaction sequence with the corresponding time scales for oxygen activation, CO translation, collisions that lead to form the TS and either dissociation back to reactants and further collisions into the TS or, with lower probability, to the final CO₂ reaction product.



Let us now address the transient populations as a function of delay time between the optical and x-ray laser pulses. Within the time resolution of the experiment, Fig. 1B shows an almost instantaneous O 1s shift to lower energy consistent with O moving from the hollow site toward the bridge site (Fig. 2C). The activation of CO is somewhat slower, where the 500 fs transient is within the time resolution of previous measurements of pure CO on Ru(0001) (15). These studies concluded that excitation of frustrated rotations (29) leads to translational motion on the surface (15).

Femtosecond laser-induced reactions are typically explained in terms of photoexcitation of substrate electrons leading to thermalized electrons at a high temperature and subsequent heating of the substrate phonons (Fig. 3A), which on ruthenium takes place on a time scale of ~1 to 2 ps (13). The reaction is thus driven via energy transfer from the electron or phonon systems to the adsorbates. The observed subpicosecond time scale is consistent with a dominating excitation process involving electrons in the substrate (13, 15, 30), with weaker coupling for the CO molecule than for O, leading to a slower response. The spectral changes associated with TS1 and the region between TS1 and TS2 in terms of the O^{*}C–O and OC–O^{*} resonances both have the same transient of 800 fs, suggesting a population of the same class of configurations. These spectral components reach a maximum in intensity after around 1 ps, as shown in Fig. 1B. Because most of the energy to reach the TS is related to the activation of the oxygen atom, we followed the contrast at the low-energy side of the spectra that decays on a time scale of a few ps (19). This indicates vibrationally excited atomic motions as in a thermal process, making the species undergo several attempts to react. The two broad overlapping components between 535 and 541 eV in the fit of the experimental spectrum indicate that there is a distribution of transient species of various OC–O bond lengths. This is further corroborated by the rather constant intensity of all observed transient species between 1 and 3 ps.

In the fit of the experimental data in Fig. 1A, there is roughly a 10% population of species in the TS region between 1.5 and 3 ps. Figure 3 demonstrates that this is consistent with a sufficiently highly excited vibrational state. Figure 3B shows the vibrational wave function probability distribution for different quantum states in the CO and

O potential well up to TS1 from Fig. 2A. Highly excited vibrational states clearly have large amplitude at the turning points where, in a classical picture, the motion slows down. We estimate the probability (19) of finding O and CO in the CO₂ TS region as indicated in Fig. 3B based on an elevated adsorbate temperature obtained from ultrafast energy transfer from transiently excited substrate electrons (19). With an estimated peak adsorbate temperature of 1500 to 3300 K (Fig. 3A), we find a transient population of the TS region up to ~10% (Fig. 3C). The majority of these species are reflected back to O and CO at the barrier but still have a significant probability of populating the vicinity of the classical turning point in the TS region. We note that CO₂ molecules formed from reactants passing over the barrier are expected to desorb with excess translational energy from a hot state rather than forming an intermediate chemisorbed state (25). The origin of the low transmission coefficient over the barrier to the CO₂ final product is an open question where friction leading to nonadiabatic processes could play an important role and will require further theoretical work.

From the above observations, we summarize the findings based on a simple picture as depicted in Fig. 4. The O becomes activated with motions parallel to the surface on a time scale below 300 fs, whereas CO is activated on a 500-fs time scale. They will start to collide on the surface because the CO is caged by O atoms in neighboring sites in the coadsorbed honeycomb structure (19). These collisions generate a transient population of species around the TS region that appears on time scales slightly longer than the initial motion of the CO and O species. Most collisions lead to dissociation back to CO and O, with subsequent further collisions into TS, and only a small fraction of the events result in the formation of CO₂ as seen in the low reaction yield (11).

We thus experimentally observe species near and beyond the rate-determining barrier at TS1, i.e., also in the rather flat region between TS1 and TS2, as shown in Fig. 2A. Although unexpected, this is not surprising given that, both classically and quantum mechanically, transit over a potential energy barrier entails a deceleration as kinetic energy is converted to potential energy. The ability to probe transient species close to the TS opens completely new insights into the electronic states of reacting molecules at surfaces, and it provides

theory with an unprecedented benchmark in the description of surface-catalyzed processes. We anticipate that this will provide an essential tool to underpin our fundamental understanding of surface chemical processes in heterogeneous catalysis.

REFERENCES AND NOTES

1. J. C. Polanyi, A. H. Zewail, *Acc. Chem. Res.* **28**, 119–132 (1995).
2. A. Stolow, A. E. Bragg, D. M. Neumark, *Chem. Rev.* **104**, 1719–1758 (2004).
3. P. I. Ionov, S. I. Ionov, C. Wittig, *J. Chem. Phys.* **107**, 9457–9463 (1997).
4. A. J. Orr-Ewing, *J. Chem. Phys.* **140**, 090901 (2014).
5. N. F. Scherer, C. Sipes, R. B. Bernstein, A. H. Zewail, *J. Chem. Phys.* **92**, 5239–5259 (1990).
6. G. Ertl, *Reactions at Solid Surfaces* (Wiley, Hoboken, NJ, 2009).
7. J. K. Nørskov, F. Studt, F. Abild-Pedersen, T. Bligaard, *Fundamental Concepts in Heterogeneous Catalysis* (Wiley, 2014).
8. H. Petek, *J. Chem. Phys.* **137**, 091704 (2012).
9. J. A. Prybyla, T. F. Heinz, J. A. Misewich, M. M. T. Loy, J. H. Glowina, *Phys. Rev. Lett.* **64**, 1537–1540 (1990).
10. F. Kao, D. G. Busch, D. Cohen, D. Gomes da Costa, W. Ho, *Phys. Rev. Lett.* **71**, 2094–2097 (1993).
11. T.-H. Her, R. J. Finlay, C. Wu, E. Mazur, *J. Chem. Phys.* **108**, 8595 (1998).
12. M. Bonn et al., *Science* **285**, 1042–1045 (1999).
13. C. Frischkorn, M. Wolf, *Chem. Rev.* **106**, 4207–4233 (2006).
14. P. Szymanski, A. L. Harris, N. Camillone III, *J. Phys. Chem. C* **112**, 15802–15808 (2008).
15. M. Beyre et al., *Phys. Rev. Lett.* **110**, 186101 (2013).
16. Dell'Angela et al., *Science* **339**, 1302–1305 (2013).
17. T. Katayama et al., *J. El. Spec. Rel. Phen.* **187**, 9–14 (2013).
18. W. F. Schlottner et al., *Rev. Sci. Instrum.* **83**, 043107 (2012).
19. Details of the materials and methods, and supporting analysis of the experimental and theoretical data, are available as supplementary materials at Science Online.
20. A. Nilsson et al., *Catal. Lett.* **100**, 111–114 (2005).
21. C. Keller et al., *Phys. Rev. B* **57**, 11951–11954 (1998).
22. E. O. F. Zdansky et al., *Phys. Rev. B* **48**, 2632–2641 (1993).
23. M. Lisowski et al., *Appl. Phys., A Mater. Sci. Process.* **78**, 165–176 (2004).
24. L. Triguero, L. G. M. Pettersson, H. Ågren, *Phys. Rev. B* **58**, 8097–8110 (1998).
25. C. Hess et al., *Appl. Phys., A Mater. Sci. Process.* **71**, 477–483 (2000).
26. H. Tillborg, A. Nilsson, N. Mårtensson, J. N. Andersen, *Phys. Rev. B* **47**, 1699–1702 (1993).
27. H. Tillborg, A. Nilsson, N. Mårtensson, *Surf. Sci.* **273**, 47–60 (1992).
28. J. Stöhr, *NEXAFS Spectroscopy*, G. Ertl, R. Gomer, D. L. Mills, Eds., Springer Series in Surface Science (Springer-Verlag, Berlin-Heidelberg, 1992).
29. M. Bonn et al., *Phys. Rev. Lett.* **84**, 4653–4656 (2000).
30. A. C. Luntz, in *Chemical Bonding at Surfaces and Interfaces*, A. Nilsson, L. G. M. Pettersson, J. K. Nørskov, Eds. (Elsevier, 2008).

ACKNOWLEDGMENTS

This work is supported by the U.S. Department of Energy, Basic Energy Science through the SUNCAT Center for Interface Science and Catalysis, the Swedish Research Council,

the Knut and Alice Wallenberg foundation, the U.S. Department of Energy through the SLAC Laboratory Directed Research and Development program under contract DE-AC02-76SF00515, the Volkswagen Stiftung, and the Deutsche Forschungsgemeinschaft within the excellence cluster "Center for Ultrafast Imaging (CUI)." The spectrum calculations were performed on resources provided by the Swedish National Infrastructure for Computing (SNIC) at the HPC2N center. Portions of this research were carried out on the SXR Instrument at the Linac Coherent Light Source (LCLS), a division of SLAC National Accelerator Laboratory, and an Office of Science user facility

operated by Stanford University for the U.S. Department of Energy. The SXR Instrument is funded by a consortium whose membership includes the LCLS, Stanford University through the Stanford Institute for Materials Energy Sciences (SIMES), Lawrence Berkeley National Laboratory (LBNL), University of Hamburg through the Bundesministerium für Bildung, Wissenschaft, Forschung und Technologie priority program FSP 301, and the Center for Free Electron Laser Science (CFEL). The experimental and theoretical data are available in the supplementary materials.

SUPPLEMENTARY MATERIALS

www.sciencemag.org/content/347/6225/978/suppl/DC1
Materials and Methods
Figs. S1 to S7
Table S1
Structures and Data
References (31–46)

26 September 2014; accepted 28 January 2015
Published online 12 February 2015;
10.1126/science.1261747

ACTUATING MATERIALS

Voxelated liquid crystal elastomers

Taylor H. Ware,^{1,2} Michael E. McConney,¹ Jeong Jae Wie,^{1,2}
Vincent P. Tondiglia,^{1,3} Timothy J. White^{1,*}

Dynamic control of shape can bring multifunctionality to devices. Soft materials capable of programmable shape change require localized control of the magnitude and directionality of a mechanical response. We report the preparation of soft, ordered materials referred to as liquid crystal elastomers. The direction of molecular order, known as the director, is written within local volume elements (voxels) as small as 0.0005 cubic millimeters. Locally, the director controls the inherent mechanical response (55% strain) within the material. In monoliths with spatially patterned director, thermal or chemical stimuli transform flat sheets into three-dimensional objects through controlled bending and stretching. The programmable mechanical response of these materials could yield monolithic multifunctional devices or serve as reconfigurable substrates for flexible devices in aerospace, medicine, or consumer goods.

The dexterity, reversibility, and reconfigurability of complex shape or surface adaptivity within soft materials may enable enhancement and miniaturization of devices in medicine, robotics, and aerospace (1). Complex shape change and actuation has been reported in patterned hydrogels and through mechanical programming of carefully designed semicrystalline polymer networks (2, 3). The implementation of programmable shape change in applications in aerospace and other outlets requires the further development of soft materials that exhibit large stimuli-induced responses while affording local control of the magnitudes and directionality of the strain. Once realized, these shape-programmable materials could enable and extend the functionality of devices in applications from as simple as packaging to as complex as deployable and tunable antennas.

Liquid crystal elastomers (LCEs) are lightly cross-linked, ordered polymers that exhibit a reversible shape change in response to heat, light, or solvent. The alignment of LCEs into so-called monodomain or single-crystal orientations has primarily used stretching [analogous to the training of shape memory metals (4)] or magnetic fields. Uniaxially aligned LCEs exhibit dimensional changes (tensile strain) that can exceed 300% along the alignment direction in response to temperature changes (5). However, these alignment methods are limited in spatial control of orientation as well as resolution. Complex director profiles within LCEs are necessary to realize monolithic

devices or functional substrates capable of non-trivial, programmable, reversible shape change (6–8). Such methods exist and have been used

to generate complex and spatial variations in the director orientations of low-molar-mass liquid crystals as well as glassy liquid crystalline polymer networks (9, 10). However, the materials chemistries and procedures used to synthesize aligned LCEs have proven insensitive to these techniques. Here, we report on the development of a facile materials chemistry platform that is conducive to the surface alignment of liquid crystals. The sensitivity of the materials chemistry to surface alignment is combined with photoalignment of volumetric elements (also known as "voxels") containing discrete domains of aligned LCEs. Enabled by the large strain inherent to LCEs, the sensitivity of the materials chemistry to surface alignment, and the optical patterning methods, we demonstrate programmable shape change and actuation in monolithic elements derived from a variety of complex director profiles.

To prepare spatially heterogeneous LCEs, we developed an optical patterning system in which

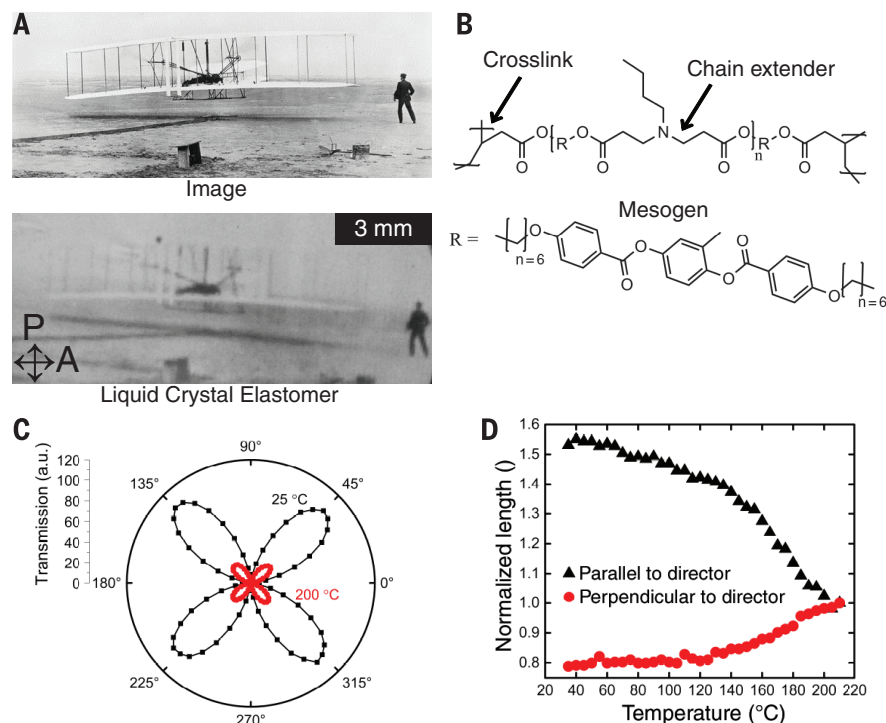


Fig. 1. Digital patterning of LCEs. (A) Liquid crystals can be aligned point-by-point by altering surface conditions. (Top) An image (29) is digitized, and the grayscale value is converted to an alignment condition. Between crossed polarizers, the programmed optical rotation of the liquid crystal introduces light and dark regions. (B) Schematic of chemical structure of the main-chain LCE that can be surface-aligned. (C) Transmission of light through an LCE between crossed polarizers in the room-temperature nematic state and high-temperature paranematic state. (D) Biaxial actuation of homogeneously aligned LCE in the absence of mechanical load.

¹Air Force Research Laboratory, Materials and Manufacturing Directorate, Wright-Patterson Air Force Base, OH, USA. ²Azimuth Corporation, Dayton, OH, USA. ³Leidos, Dayton, OH, USA.

*Corresponding author. E-mail: timothy.white.24@us.af.mil